A Tale of Two Clusters: An Analysis of Gas-phase Metallicity and Nebular Gas Conditions in Proto-cluster Galaxies at $z \sim 2$

Leo Y. Alcorn[1,2,11], Anshu Gupta[3,4], Kim-Vy Tran[1,2,3,4], Glenn G. Kacprzak[4,5], Tiantian Yuan[4,5], Jonathan Cohn[1,2], Ben Forrest[6], Karl Glazebrook[5], Anishya Harshan[3], Lisa J. Kewley[4,7], Ivo Labbé[5], Themiya Nanayakkara[8], Casey Papovich[1,2], Lee R. Spitler[9], and Caroline M. S. Straatman[10]

[1] Department of Physics and Astronomy, Texas A&M University, College Station, TX 77843-4242, USA; lyalcorn@tamu.edu
[2] George P. and Cynthia Woods Mitchell Institute for Fundamental Physics and Astronomy, Texas A&M University, College Station, TX 77843-4242, USA
[3] School of Physics, University of New South Wales, Sydney, NSW 2052, Australia
[4] ARC Centre of Excellence for All Sky Astrophysics in 3 Dimensions (ASTRO 3D), Australia
[5] Swinburne University of Technology, Hawthorn, VIC 3122, Australia
[6] Department of Physics & Astronomy, University of California, Riverside, 900 University Avenue, Riverside, CA 92521, USA
[7] Research School of Astronomy and Astrophysics, The Australian National University, Cotter Road, Weston Creek, ACT 2611, Australia
[8] Leiden Observatory, Leiden University, P.O. Box 9513, NL 2300 RA Leiden, The Netherlands
[9] Department of Physics and Astronomy, Faculty of Science and Engineering, Macquarie University, Sydney, NSW 2109, Australia
[10] Sterrenkundig Observatorium, Universiteit Gent, Krijgslaan 281 S9, B-9000 Gent, Belgium

Abstract

The ZFIRE survey has spectroscopically confirmed two proto-clusters using the MOSFIRE instrument on Keck I: one at $z = 2.095$ in COSMOS and another at $z = 1.62$ in UKIRT Infrared Deep Sky Survey (UDS). Here, we use an updated ZFIRE data set to derive the properties of ionized gas regions of proto-cluster galaxies by extracting fluxes from emission lines Hβ 4861 Å, [O III] 5007 Å, Hα 6563 Å, [N II] 6585 Å, and [S II] 6716,6731 Å. We measure gas-phase metallicity of members in both proto-clusters using two indicators, including a strong-line indicator relatively independent of the ionization parameter and electron density. Proto-cluster and field galaxies in both UDS and COSMOS lie on the same Mass–Metallicity Relation with both metallicity indicators. We compare our results to recent IllustrisTNG results, which report no significant gas-phase metallicity offset between proto-cluster and field galaxies until $z = 1.5$. This is in agreement with our observed metallicities, where no offset is measured between proto-cluster and field populations. We measure tentative evidence from stacked spectra that indicate UDS high-mass proto-cluster and field galaxies have differing [O III]/Hβ ratios; however, these results are dependent on the sample size of the high-mass stacks.

Key words: galaxies: clusters: general – galaxies: evolution – galaxies: high-redshift

1. Introduction

Proto-clusters are the precursors to the most extreme environments in the universe. In the local universe ($z = 0$), there is a relationship between environmental density and the properties of galaxies, i.e., morphology, stellar populations, and star-formation rate (SFR). In particular, studies have found elevated gas-phase metallicity in Local Cluster galaxies (Cooper et al. 2008; Ellison et al. 2009), lower SFRs in cluster galaxies (Lewis et al. 2002; Grootes et al. 2017; Jarrett et al. 2017), a greater fraction of elliptical and lenticular galaxies in denser environments (Houghton 2015), redder colors with increasing density (Blanton et al. 2005), and a higher fraction of slow rotating galaxies in dense environments (Cappellari et al. 2011). Since cluster environments show these correlations at low redshift ($z < 0.5$), we wish to observe when the environment-dependent evolution of galaxies unfolds. At higher redshifts, the number fraction of low-SFR and quenched galaxies in denser environments decreases (Nantais et al. 2013; Lee et al. 2015; Kawinwanichakij et al. 2017; Pintos-Castro et al. 2019), until the SFR density of the universe reaches its peak at $z \sim 2$ (Hopkins & Beacom 2006; Madau & Dickinson 2014).

The period known as "Cosmic Noon" ($1.5 < z < 2.5$) is of particular interest, as this is the stage where massive galaxies

within proto-clusters are rapidly building their stellar populations (Tran et al. 2010; Hatch et al. 2011; Koyama et al. 2013a; Lee et al. 2015; Shimakawa et al. 2018). Analyses of metallicity (Kacprzak et al. 2015, 2016; Kulas 2013; Magrini et al. 2012; Shimakawa et al. 2015; Tran et al. 2015; Valentino et al. 2015), star formation (Koyama et al. 2013a, 2013b; Tran et al. 2015, 2017), ionized gas characteristics (Kewley et al. 2016), gas content (Koyama et al. 2017; Darvish et al. 2018), and kinematics (Alcorn et al. 2016, 2018) of proto-cluster members at $z > 1.5$ showed no strong ($>2\sigma$) offsets compared to field galaxies at the same epoch. Some studies of galaxy sizes in proto-clusters versus field populations observe an increase in proto-cluster star-forming galaxy (SFG) sizes relative to the field (Allen et al. 2015; Ito et al. 2019), but others do not observe a difference (Rettura et al. 2010; Bassett et al. 2013; Suzuki et al. 2019). Clear signatures of the morphology and color relation in dense environments have been observed in Cooper et al. (2006), Gobat et al. (2011), Papovich et al. (2012), Bassett et al. (2013), and Strazzullo et al. (2016). Additionally, an increase in merger rates in $z \sim 2$ clusters were observed (Lotz et al. 2013; Watson et al. 2019).

Cosmological simulations have found small (0.05–0.1 dex) metallicity enhancements in proto-clusters at $z > 1.5$. The simulations by Davé et al. (2011) determined a metallicity enhancement in galaxies in dense environments on the order of ~0.05 dex. Kacprzak et al. (2015) performed hydrodynamical

---

simulations with Gadget-3 (Kobayashi et al. 2007), determining that proto-cluster galaxies at $z \sim 2$ would be enhanced by $\sim$0.1 dex from field galaxies in the Mass–Metallicity Relation (MZR). Gupta et al. (2018) observed that within the IllustrisTNG (100 Mpc)^3 simulation (TNG100), galaxies in proto-clusters show a $\sim$0.05 dex gas-phase metallicity enhancement compared to field galaxies starting at $z = 1.5$, but no significant offsets at $z = 2$ and higher. This possibly identifies the redshift when the cluster environment starts influencing member galaxies in terms of their gas-phase metallicities. Here, we provide an observational counterpart to the Gupta et al. (2018) IllustrisTNG results and determine the gas-phase metallicity offset between two proto-cluster populations and field galaxies at $z = 1.6$ and 2.095.

The ZFIRE survey (Tran et al. 2015; Nanayakkara et al. 2016) spectroscopically confirmed the over-dense region in the COSMOS field at $z = 2.095$ (Yuan et al. 2014), and the over-dense region in the UDS field at $z = 1.62$ (Papovich et al. 2010; Tran et al. 2015). With the ZFIRE data set of $z \sim 2$ proto-cluster galaxies, it is possible to extend kinematic and metallicity scaling relations to the proto-cluster environment at $z \sim 2$. The ZFIRE data set allows us to examine the interplay of the intra-cluster medium, galactic winds, and the interstellar medium (ISM) in a cluster and its member galaxies. The proto-clusters observed in this study were originally identified using deep NIR imaging in Papovich et al. (2010) and Spitler et al. (2012). Using rest-frame optical emission lines from members of the proto-cluster, we can directly compare nebular gas properties of cluster and field populations at this epoch.

The ZFIRE collaboration has increased its sample since the initial data release in both the UDS and COSMOS fields, and has measured more nebular emission lines (Hβ, [O III]) from galaxies in the previous sample (Tran et al. 2015; Nanayakkara et al. 2016). The extended sample allows us to perform a re-analysis (originally by Kewley et al. 2016) of the Baldwin–Phillips–Terlevich (BPT) Diagram (Baldwin et al. 1981) on the basis of redshift, inferred stellar mass, and environmental density. The sample of COSMOS galaxies with all BPT diagnostic emission lines is doubled (from 37 galaxies to 74), and 41 UDS galaxies are also analyzed using the BPT Diagram. Additionally, we stack spectra not seen in the previous BPT (Kewley et al. 2016) or MZR (Kacprzak et al. 2015; Tran et al. 2015) studies. This diagnostic will provide information on the nebular gas in each proto-cluster to determine if star-forming conditions evolve with redshift.

By including recent improvements in gas-phase metallicity indicators, we will re-examine galaxy metallicity and directly compare two proto-clusters at $z \sim 2$ to the field. Gas-phase metallicity values for the same galaxy can differ between metallicity indicators by up to one order of magnitude (Kewley & Ellison 2008). Discrepancies between different strong-line indicators are possibly the result of the calibration on local H II regions, which depends on the measurement of electron temperature (Pilyugin & Thuan 2005; Pilyugin & Mattsson 2011; Maiolino & Mannucci 2019). Calibrations using local H II regions can be flawed when used for high-redshift measurements, because possible changes in the nebular gas properties of high-redshift galaxies have been observed compared to local galaxies. In particular, galaxies at high redshift have been observed to have higher ionization parameters and electron densities than local galaxies

(Brinchmann et al. 2008; Liu et al. 2008; Lehnert et al. 2009; Newman et al. 2012, 2014; Kewley et al. 2013; Tacconi et al. 2013; Shirazi et al. 2014; Steidel et al. 2014, 2016; Shapley et al. 2015; Kaasinen et al. 2018; A. Harshan et al. 2019, in preparation).

We utilize the strong-line gas-phase metallicity diagnostics introduced in Pettini & Pagel (2004, referred to herein as PP04) and the newer indicator by Dopita et al. (2016, referred to as D16). The PP04 indicator is widely used in high-redshift extragalactic astronomy (Wuyts et al. 2014; Zahid et al. 2014; Sanders et al. 2015, 2018) and is not sensitive to reddening (because it utilizes a ratio of Hα to [N II]). However, it is subject to the calibration issues noted above and is sensitive to the ionization parameter and electron density of a host galaxy, as well as the presence of shock-heated gas and low-level active galactic nuclei (AGNs). The D16 indicator attempts to correct this by including the [S II] doublet in this ratio, and photoionization models show that it is insensitive to ionization parameter and electron density. We measure gas-phase metallicity using both strong-line indicators in this study to determine the effectiveness of the D16 indicator.

In Section 2, we review our data from *Magellan* (FOUR-STAR) and Keck (MOSFIRE) and extensive public multi-wavelength observations. We discuss our line-fitting and flux extraction methods in Section 3, including both individual objects (Section 3.1) and stacked emission lines (Section 3.2). Our results for gas-phase metallicity between proto-cluster and the field in UDS and COSMOS are shown in Section 4.1. The nebular gas analysis of individual galaxies and our stacked objects using the BPT diagram is located in Section 4.2. Finally, our results are put into the context of galaxy evolution in the proto-cluster environment in Section 5.

In this work, we assume a flat ΛCDM cosmology with $\Omega_M = 0.3$, $\Omega_\Lambda = 0.7$, and $H_0 = 70$. At the COSMOS proto-cluster redshift, $z = 2.095$, one arcsecond corresponds to a proper angular scale of 8.33 kpc. At the UDS proto-cluster redshift, $z = 1.62$, one arcsecond corresponds to a proper angular scale of 8.47 kpc.

2. Data

2.1. Sample Selection

Our proto-cluster and field samples are drawn from the ZFIRE survey, a spectroscopic follow-up of ZFOURGE observations (Straatman et al. 2016). ZFOURGE combines broadband imaging in K_s and the medium-band J_1, J_2, J_3, H_s, and H_l filters to select objects using K_s-band images with an 80% completeness limit of 25.5 and 25.8 AB magnitudes in the COSMOS and UDS fields, respectively.[12] Rest-frame UVJ colors are used to identify SFGs, which should have prominent nebular emission lines. We account for AGNs using the Cowley et al. (2016) AGN catalog.

ZFOURGE uses FAST (Kriek et al. 2009) to fit Bruzual & Charlot (2003) stellar population synthesis models to the galaxy spectral energy distributions and estimate observed galaxy properties. We calculated stellar masses with FAST using the spectroscopic redshift from MOSFIRE (Nanayakkara et al. 2016). We assume a Chabrier (2003) initial mass function with constant solar metallicity and an exponentially declining SFR, and a Calzetti et al. (2000) dust law. For a full summary, see Tran et al. (2015), Nanayakkara et al. (2016), and Straatman et al. (2016).

---

[12] http://zfourge.tamu.edu/

2.1.1. UDS

The UDS proto-cluster at $z = 1.62$ was identified by Papovich et al. (2010) and Tanaka et al. (2010), from the Williams et al. (2009) catalog of UDS, a subset of the UKIRT survey (Lawrence et al. 2007). A ZFIRE analysis of the UDS proto-cluster identified 26 confirmed proto-cluster members between $1.6118 < z < 1.6348$, and 36 field galaxies at equivalent redshifts (Tran et al. 2015). This proto-cluster was shown to have a strikingly low velocity dispersion of $\sigma_{cl} = 254 \pm 50$ km s^{-1} (Tran et al. 2015), and notably showed an increase in star formation with local density (Tran et al. 2010). Previous studies of this proto-cluster showed no enhancement in gas-phase metallicity (using the PP04 indicator, commonly referred to as N2 in literature) or attenuation compared to field samples (Tran et al. 2015).

2.1.2. COSMOS

The COSMOS proto-cluster was initially identified in Spitler et al. (2012) using photometric redshifts from ZFOURGE and confirmed with spectroscopic redshifts from MOSFIRE (Yuan et al. 2014). This over-density consists of four merging groups and is projected to evolve into a Virgo-like cluster at $z = 0$ (Yuan et al. 2014). Fifty-seven cluster members are identified to spectroscopic redshifts within $2.08 < z < 2.12$, and the cluster velocity dispersion was shown to be $\sigma_{cl} = 552 \pm 52$ km s^{-1}. This proto-cluster shows no enhancement in PP04 gas-phase metallicity compared to field samples (Kacprzak et al. 2015). One hundred twenty-three star-forming field galaxies are selected from redshifts of $2.0 < z < 2.5$ from ZFIRE photometric modeling.

2.2. MOSFIRE NIR Spectroscopy

Observations were taken in 2013 December, 2014 February, 2016 January, and 2017 February in the H and K filters covering 1.47–1.81 μm and 1.93–2.45 μm, respectively. Seeing varied from $\sim 0.''4$ to $\sim 1.''3$ over the course of our observations. Galaxies (star-forming, dusty, and quiescent) in over-dense regions in COSMOS and UDS were prioritized for observation over star-forming field galaxies. For further information on target selection, see Nanayakkara et al. (2016).

The spectra are flat fielded, wavelength calibrated, and sky subtracted using the MOSFIRE data reduction pipeline (DRP).[13] A custom ZFIRE pipeline corrected for telluric absorption and performed a spectrophotometric flux calibration using a type A0V standard star. We flux calibrate our objects to the continuum of the standard star and use ZFOURGE photometry as an anchor to correct offsets between photometric and spectroscopic magnitudes. The final result of the DRP are flux-calibrated 2D spectra and 2D 1σ images used for error analysis with a flux calibration error of $<10\%$ (~ 0.08 mag). For more information on ZFIRE spectroscopic data reduction and spectrophotometric calibrations, see Nanayakkara et al. (2016).

3. Methods

3.1. Emission-line Flux Measurements

We obtain emission-line fluxes from our telluric-corrected and flux-calibrated spectra by fitting Gaussian profiles to

---

[13] http://keck-datareductionpipelines.github.io/MosfireDRP

emission lines. Our 2D spectra are collapsed to a 1D spectrum by fitting a Gaussian to the spatial line profile and summing along an aperture where each edge is twice the FWHM away from the center of the spatial profile of the emission line. We then fit a Gaussian profile to the 1D spectrum of the emission line. In Figure 1, it is clear that the [S II] lines are well resolved and not blended; therefore, we fit two single Gaussian profiles simultaneously at a fixed distance between their centroids.

3.1.1. Measuring Profiles

From the best-fit profile to the emission line, the standard deviation of the Gaussian is used to determine the range over which the line will be integrated, and we sum under the best-fit Gaussian from $-3\sigma < \lambda_{obs} < 3\sigma$, where $\sigma = $ FWHM$/2.35482$. This value is our extracted flux measurement. We measure noise by summing the error spectrum in quadrature over the same bounds as the signal. For faint emission lines ([N II], [S II], Hβ), we fit the line holding the Gaussian σ fixed to the σ measurement of the Hα line (for [N II] and [S II]) or the [O III] emission line (for Hβ). If the emission line of an object is less than $2\times$ the measured noise in its region, we mark this object as an upper limit of the signal (unfilled points on Figure 2) and use the 1σ noise limit as our flux detection.

3.1.2. Contamination by Sky Lines

Due to strong sky emission-line interference, we extracted only one UDS galaxy and 13 COSMOS galaxies with Hα, [N II], and [S II] unaffected by significant sky noise. However, 13 UDS galaxies and 47 COSMOS galaxies were extracted with upper limits due to sky emission. Galaxies with Hα, [N II], and [S II] fluxes were used for our gas-phase metallicity analysis in Section 4.1. For our flux ratio analysis (Section 4.2), we extracted fluxes for 26 COSMOS galaxies with Hβ, [O III], Hα, and [N II] emission lines (15 of which had no emission lines with sky interference and 11 of which had at least one emission line with sky interference). We also extracted fluxes for 11 UDS galaxies with all emission lines (5 with no sky interference, 6 with at least one emission line with sky interference). We rejected objects with an emission-line signal-to-noise ratio (S/N) < 2, which we discuss further in Section 4.1.1.

3.2. Stacking Emission Lines

As many of our galaxies have very faint emission lines (i.e., [N II], Hβ, [S II]), we stack our galaxy spectra into bins of stellar mass and environment to determine characteristics of their populations. The stacked spectra include galaxies with emission line S/N < 2, in contrast to our analysis with individual galaxies. Spectra are collapsed over the same spatial aperture as determined in Section 3.1, then normalized to the Hα flux or [O III] flux, depending on the filter observed. Objects are then interpolated onto a reference rest wavelength range preserving flux. We take the median value of our stacks after rejecting outlier pixels with values greater than the median ± 3 Normalized Median Absolute Deviation (NMAD). We perform our Gaussian line-fitting procedure from Section 3.1 to determine the stacked fluxes.

To separate the effects of AGNs, we bin the objects identified as AGNs in Cowley et al. (2016). AGNs are displayed separately in our BPT diagrams for reference. Cowley et al. (2016) identifies AGNs in the ZFOURGE sample using radio, IR, UV, and X-ray
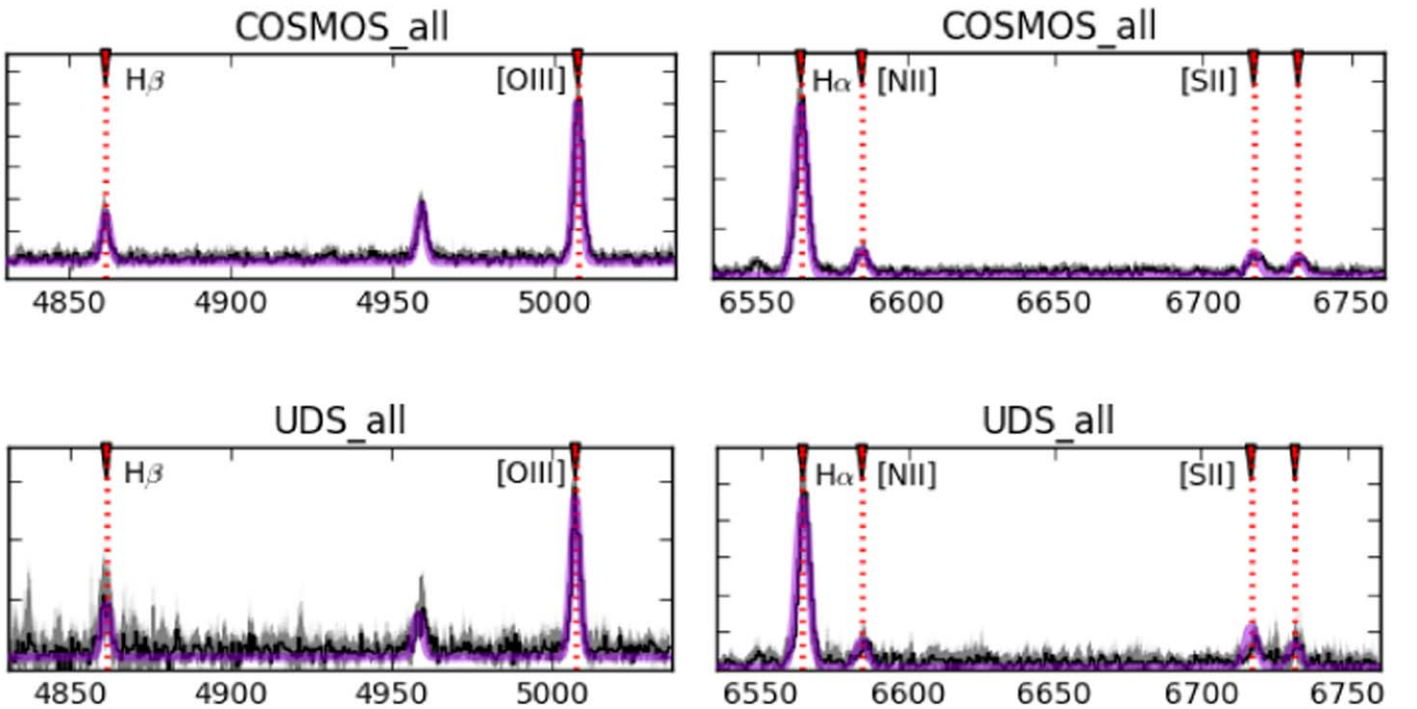
Figure 1. Stacked rest-frame spectra of our sample, showing Hα, [N II], [S II], Hβ, and [O III]. The stacked spectra are shown in black and have been outlier-rejected. The pink lines show the best-fit Gaussian profiles for the measured emission lines. We show the individual bootstrapped spectra used for determining errors in gray. The red arrows at the top of each spectrum point to the measured emission lines. Left panels: the stacked [O III] and Hβ emission lines. In COSMOS, these lines are observed in the MOSFIRE *H* band. In UDS, these lines are observed in the MOSFIRE *J* band. Right panels: the stacked Hα, [N II], and [S II] emission lines. In the COSMOS sample, these lines are observed in the *K* band, and in the UDS sample in the *H* band. The Gaussian fits are used to measure stacked flux ratios.

data. AGNs can affect placement on the BPT diagram as the emission is from shocked gas or photoionization by the hard ionizing spectrum of the AGN, rather than gas photoionized by young stellar populations.

We stack our objects based on mass, environment, field (COSMOS versus UDS), and detected AGNs. Objects are separated by (i) low ($M_\star < 9.60$) versus high ($M_\star > 6$) stellar-mass objects, where $M_\star = 6$ is the median stellar mass of the COSMOS sample, and (ii) objects identified within each proto-cluster (from the redshift limits of each proto-cluster) versus objects that are field galaxies (See Sections 2.1.1 and 2.1.2).

4. Results

4.1. Gas-phase Metallicity

4.1.1. Comparing Strong-line Indicators

We apply the strong-line diagnostic presented in Dopita et al. (2016) to determine gas-phase metallicities for a sample of our galaxies (Figure 2, right panels). This indicator requires measurements of the Hα, [N II], and [S II] emission lines. In the MOSFIRE *K* band, this indicator can be used for galaxies between $1.8 < z < 2.6$. In the *H* band, it can be used for galaxies between $1.2 < z < 1.8$. We can observe these lines for most of our objects in the same band on MOSFIRE; therefore, absolute fluxes are not required.

However, the [S II] doublet is quite faint ($\sim10^{-18}\,\mathrm{erg\,s^{-1}\,cm^{-2}/\mathring{A}}$) for most objects in our sample, and in many of our objects, we can only determine an upper bound of metallicity. The [S II] doublet may only be slightly above the noise level; because of this, we have introduced an S/N cut of 2 on all emission lines. Telford et al. (2016) showed that introducing S/N cuts can bias strong-line metallicity

measurements depending on the choice of emission lines. They determined that S/N cuts on the [N II] line will bias the sample against low-metallicity galaxies, but cuts on Hα and [S II] do not bias samples. Therefore, we are biased toward high-metallicity galaxies, but this will be seen in both metallicity indicators we discuss because both rely on measurements of [N II].

Additionally, in the UDS sample, the [S II] 6731 Å emission line is in a region of high sky interference, so we mark most of our UDS objects as having unreliable Dopita et al. (2016) metallicities. We mark objects with sky interference as unfilled points in Figure 2. When we perform the same analysis using only objects with all emission lines in low sky regions, we find that our COSMOS results are not significantly changed. Only one UDS galaxy did not have any sky emission interference in the [S II] lines, so we were not able to test this effect on the UDS population.

For comparison, we also determine metallicities from the PP04, also referred to as N2, indicator (Pettini & Pagel 2004; see Figure 2, left panels). We find that at lower values of metallicity $12 + \log(\mathrm{O/H}) < 8.25$, the PP04 indicator predicts higher metallicity values than the D16 method, possibly indicating a floor on measurement sensitivity at low metallicity due to flux limitations on the faint [N II] emission line (Figure 3). The predicted D16 indicator typically is ~0.5 dex higher than the PP04 indicator at low masses, $\log(M_* < 9.5$. Additionally, we compared our measurements to the MOSDEF sample (Sanders et al. 2018) and the previous measurements of the COSMOS proto-cluster and field Kacprzak et al. (2015), which only used the PP04 indicator, and found similar results as our PP04 measurements (Figure 2, top panels).
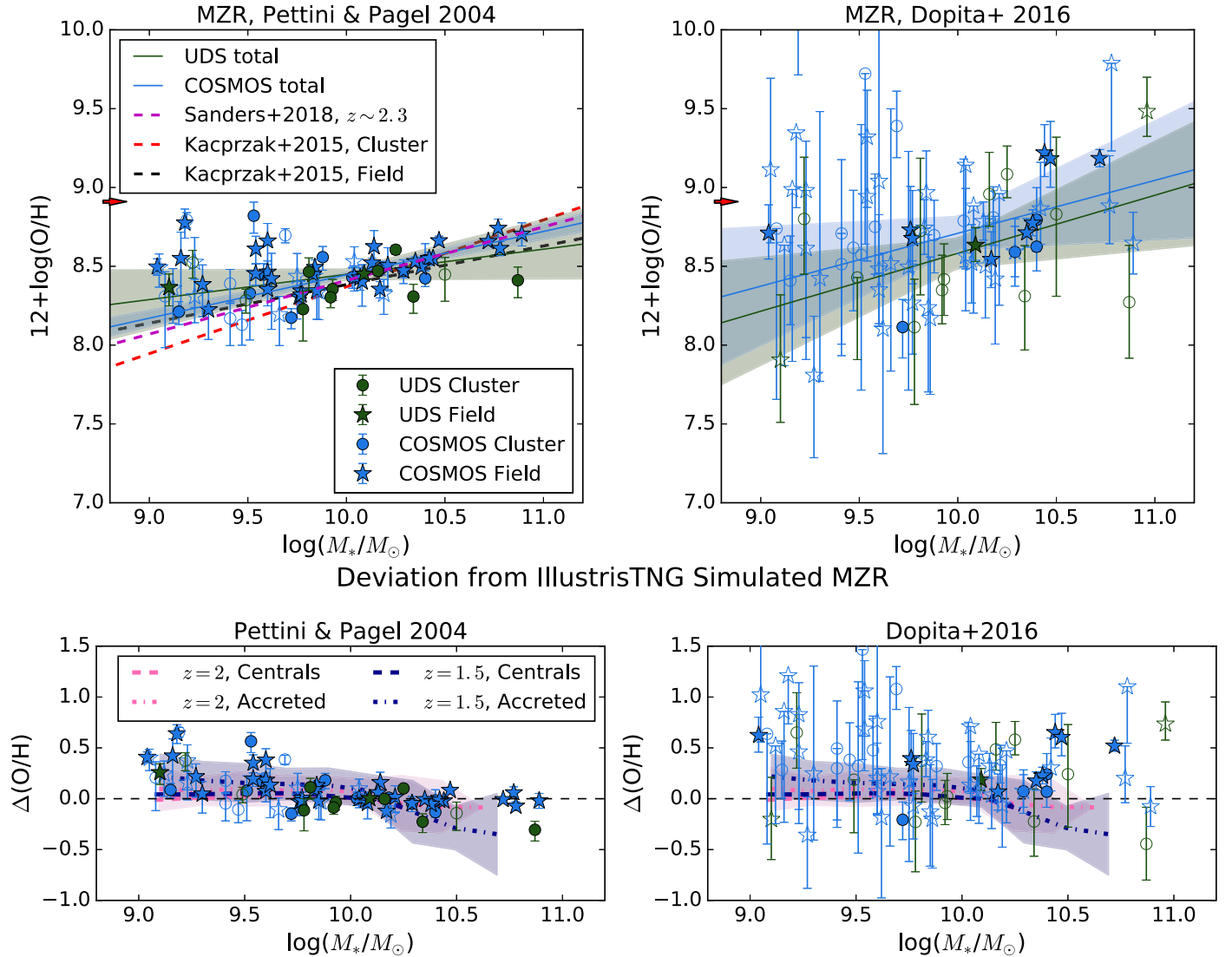
Mass Metallicity Relation (MZR)

Deviation from IllustrisTNG Simulated MZR

Figure 2. Top left panel: metallicity values determined by the indicator presented in Pettini & Pagel (2004). All emission lines are above a 2σ detection limit. When at least one emission line shows significant sky interference, the point is unfilled. We compare to the MOSDEF metallicity measurements (Sanders et al. 2018) at $z \sim 2.3$, and to the ZFIRE measurements of the COSMOS proto-cluster and field in Kacprzak et al. (2015). The small red arrows on the left side of each plot mark the location of solar metallicity. Top right panel: metallicity values determined by the indicator presented in Dopita et al. (2016). We show our best-fit linear relations for UDS and COSMOS in their respective colors. Bottom panels: we plot the offset from the slope of the MZR in the IllustrisTNG simulation. The pink and blue dotted and dashed lines are theoretical measures of the MZR from the Illustris simulation (Gupta et al. 2018; Torrey et al. 2018). The centrals are galaxies in the center of their own dark-matter potential (equivalent to a field sample), and accreted galaxies are equivalent to a cluster sample. We plot the deviation from the MZR predicted in IllustrisTNG with respect to $z = 2$ centrals (black dashed line).

Despite this observational difficulty, the strength of the D16 diagnostic is its independence from ionization parameter and ISM pressure, both of which have been shown to differ between local galaxy populations and those at high redshift (Kewley et al. 2013, 2015; Steidel et al. 2014; Shapley et al. 2015). Both the D16 and PP04 strong-line indicators depend on the correct calibration of the N/O ratio. Current estimates of the N/O ratio at high-z show identical values to local ratios, but at increased scatter (Steidel et al. 2016; Maiolino & Mannucci 2019).

There is a large difference in scatter between the two metallicity indicators (Figure 3). The NMAD scatter from the PP04 method (0.11 dex for COSMOS and 0.16 dex for UDS) is much lower than D16 (0.27 dex for COSMOS and

0.49 dex for UDS), most likely because there are fewer low-flux emission lines needed for the PP04 measurement. [S II] is a very faint emission-line doublet, and for many of our galaxies, we extracted flux limits rather than fluxes. Additionally, the [S II] line 6731 Å in the UDS proto-cluster is located in a high sky-noise region, making flux extraction difficult, and we can only extract flux upper limits. This likely explains the high scatter and super-solar metallicity values.

Because of sky emission that affects the extraction of [S II] for the D16 indicator, we find that PP04 is the better indicator for gas-phase metallicity at $z \sim 2$. We emphasize that the D16 indicator is a powerful metallicity indicator and is relatively insensitive to the changing ionized gas properties of galaxies at high redshift. Higher-S/N emission lines of galaxies
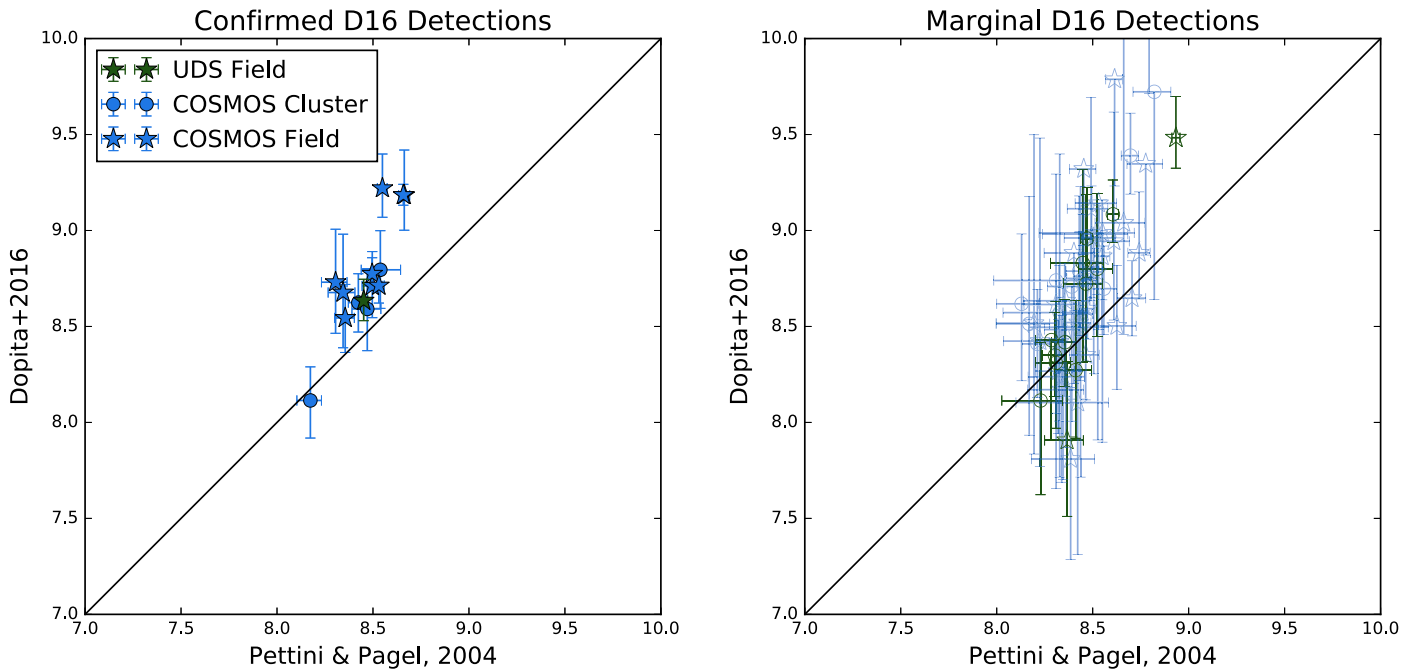
Figure 3. The direct comparison between metallicity indicators D16 (Dopita et al. 2016) and PP04 (Pettini & Pagel 2004). Colors are the same as in Figure 2. Left panel: detections where Hα, [N II], and [S II] emission lines are all free of significant sky interference. The one-to-one line, where measurements are equal, is the solid black line. Right panel: detections where at least one emission line has significant sky interference. COSMOS galaxies are made transparent so UDS galaxies can be easily viewed.

at $z \sim 2$ are needed to determine the gas-phase metallicities at the precision necessary to separate cluster and field populations. Spectra from the upcoming 30 meter class telescopes and space-based spectra (from, e.g., *JWST*) will be valuable resources.

4.1.2. Environment and Metallicity

We find consistent results to the previous ZFIRE analysis of metallicity (Kacprzak et al. 2015), which determined that the COSMOS $z = 2.095$ proto-cluster shared the same MZR as the field galaxies. In Tran et al. (2015), the UDS $z = 1.62$ proto-cluster lacked evidence of a gas-phase metallicity offset from the field sample of Steidel et al. (2014). We find here that these proto-clusters also share the same MZR and show no strong environmental influences. Our results, given the scatter in our relations, are only sensitive to a metallicity difference of about 0.15 dex for the Pettini & Pagel (2004) indicator and 0.5 dex for the Dopita et al. (2016) indicator.

When we stack our galaxies by environment and stellar mass (see Figure 4), we find the similar results. The MZR of proto-cluster and field populations are consistent within error, except in some very low-number bins (in the UDS population). Like the theoretical values shown in the lower panels of Figure 2 at $z = 1.5$ and $z = 2$, we find no strong offsets between proto-cluster and field in gas-phase metallicity.

4.1.3. Predictions from IllustrisTNG

We perform the first comparison of the gas-phase mass–metallicity relation as a function of environment to simulated results from IllustrisTNG. IllustrisTNG determined gas-phase MZRs for $0 < z < 2$ (Gupta et al. 2018; Torrey et al. 2018), and we find agreement with these predictions. The IllustrisTNG accreted/satellite galaxies were chosen from those living in

halos of $10^{13} M_\odot/h$ and above at $z = 0$, giving a total of 127 clusters. The field/central sample was chosen from galaxies within their own dark-matter halos of $10^{12.0} M_\odot/h$ at $z = 0$, and with SFR > 0. Additionally, a stellar mass limit of 10^9–$10^{10.5} M_\odot/h$ was imposed on all galaxies in the simulated sample.

Gupta et al. (2018) found that IllustrisTNG galaxies in clusters (accreted galaxies) at $z < 1$ have an MZR metallicity enhancement of 0.15–0.2 dex from field galaxies (central galaxies) at the same redshifts. At $z = 1.5$, the predicted enhancement is only 0.05 dex, and at $z = 2$ there is no enhancement. At all redshifts, Gupta et al. (2018) reports a scatter in the MZR of 0.2 dex. In the lower panels of Figure 2, we show the metallicity offset from the IllustrisTNG MZR relation for central galaxies (central galaxies within their dark-matter halo, similar to our field galaxies) and accreted galaxies (in-falling galaxies in a dark-matter halo belonging to another galaxy, equivalent to our proto-cluster galaxy samples) at $z = 2$. We can confirm that in both populations at $z = 1.62$ and $z = 2.095$, proto-cluster galaxies do not have significantly enhanced metallicities (Figure 2, lower panels, Figure 4).

The scatter of the IllustrisTNG simulated MZR remains consistent at all environments and redshifts, at a level of 0.2 dex. The scatter in our observed MZR values is only slightly smaller than the predicted scatter of the PP04 indicator in IllustrisTNG (∼0.1–0.15 dex) but larger when using the D16 indicator (∼0.3–0.5 dex). Therefore, we are unlikely to detect the minor (<0.05 dex) MZR enhancement seen at $z > 1.5$ in the IllustrisTNG cluster galaxies.

4.2. BPT Diagram

A subset of our galaxies in both proto-clusters have measurements of all emission lines necessary to apply Baldwin–Phillips–Terlevich (BPT) Diagnostics (Baldwin et al. 1981).
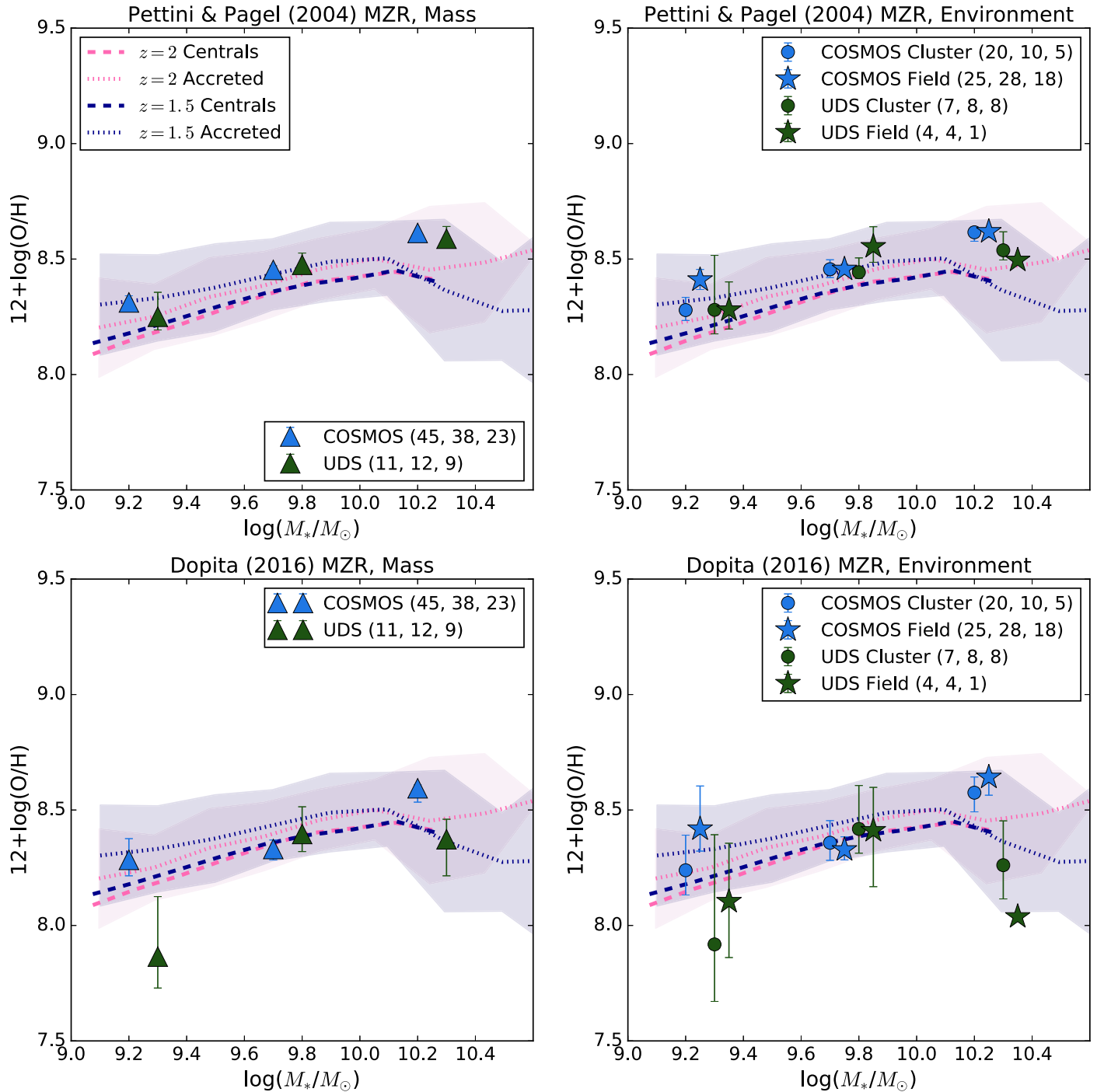
Figure 4. The stacked metallicity measurements from the sample. The top panels show metallicities determined from the indicator presented in Pettini & Pagel (2004), and the bottom panels show metallicities determined from the indicator in Dopita et al. (2016). Mass bins are offset in the $M_\star$ axis for clarity. The IllustrisTNG simulations are shown in pink and blue, with scatter shown in shaded regions. Central galaxies are simulated galaxies that are central within their dark-matter halos, equivalent to our field sample. Accreted galaxies are in-falling galaxies, equivalent to our cluster galaxy sample. Left panels: metallicity values binned by mass. The low-mass bin includes galaxies with $\log(M_\star) < 9.54$, the medium-mass bin from $9.54 < \log(M_\star) < 10.1$, and the high-mass bin from $\log(M_\star) > 10.1$. The legend displays the number of galaxies in low-, medium-, and high-mass bins, respectively. Right panels: metallicity binned by environment and mass.

These emission lines are Hβ 4861 Å, [O III] 5007 Å, Hα 6563 Å, and [N II] 6585 Å. We require our detections for all lines to be at an S/N > 2.

UDS galaxies appear to be offset from the COSMOS sample in the BPT diagram (Figure 5). However, the Hβ line in UDS is

located in a high sky-noise region, so our study may be biased toward objects with higher Hβ flux. A two-population Kolmogorov—Smirnov test confirms that, at a level of 0.005, that the COSMOS sample has a higher $\log([O III]/H\beta)$ ratio than the UDS sample (at a *p*-value of 0.0013). Deeper
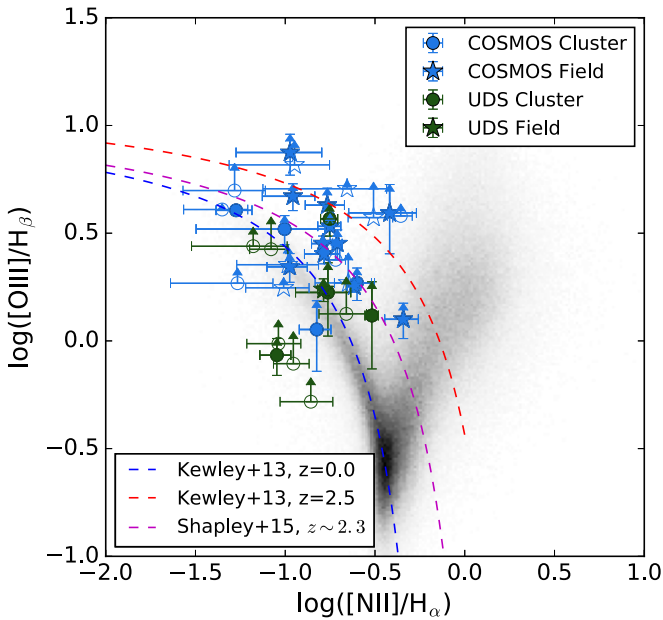
Figure 5. BPT diagram of galaxies within our two fields (COSMOS and UDS). Galaxies with all four emission lines Hα, [N II], Hβ, and [O III] with greater than 2σ detection limit are shown. Galaxies with one or more emission lines with heavy sky interference are unfilled points. Colors and marker shapes are the same as in Figure 2. Shaded regions are SDSS galaxies. Colored curves from Kewley et al. (2013) are the upper limits to the theoretical evolution of star-forming galaxies at $z = 0$ and $z = 2.5$.

observations may be necessary to determine if sky interference is biasing this analysis; however, our BPT KS test results hold when we reject objects where any emission line displays significant sky interference (Figure 5).

ISM conditions are known to change in high-redshift SFGs compared to local SFGs (Kewley et al. 2013, 2015; Shapley et al. 2015). Evolution of the ionization parameter (the amount of ionization a luminous source can produce in an H II region) does not evolve significantly between $0 < z < 1$ (Paalvast et al. 2018), but changes to more extreme ionizing conditions between $1 < z < 3$. Additionally, changes in the log([O III]/Hβ) ratio can be caused by changes in electron density, hardness of the ionizing field, and metallicity (Kewley et al. 2015). Our results indicating an offset between the COSMOS and UDS proto-cluster show a tendency in the $z = 2.095$ population to have more extreme ISM conditions than the $z = 1.62$ population. Additionally, both COSMOS and UDS offset from the SDSS sample in [O III]/Hβ (Figure 5), consistent with an evolution in ionization parameter from local galaxies.

4.2.1. Stacked BPT Measurements

Our stacked results tell a similar story (Figure 6). Galaxies are binned according to stellar mass (inferred from FAST), environment, AGN status (confirmed AGNs are excluded from the sample but shown Figure 6), and subdivided into low and high stellar-mass bins for each proto-cluster and field sample. Spectra within a bin are then stacked. In each case, the stellar mass has a strong influence on the position of stacked sample in the BPT diagram.

Higher stellar mass is known to correlate with higher metallicity and therefore higher [N II]/Hα. We can confirm this correlation with the stacked spectra in the upper right panel of Figure 6. Very clearly, there is a sequence of increasing log

([N II]/Hα) ratio with stellar mass in both the COSMOS (blue triangles) and UDS (green triangles) samples.

4.2.2. UDS (z = 1.6) versus COSMOS (z = 2.1)

In the upper left panel of Figure 6, we see galaxies in COSMOS and UDS binned purely by cluster status. The COSMOS proto-cluster (blue solid circle) is offset from the field (blue solid star) by $\sim$0.35 dex in log([N II]/Hα), and no significant log([O III]/Hβ) offset. The log([N II]/Hα) offset is likely due to the difference in median mass between cluster and field populations. The median mass of proto-cluster galaxies in COSMOS is log($M_\star$) = 9.46, and the median mass of the field galaxies is log($M_\star$) = 9.75. The UDS proto-cluster (green solid circle), in contrast, shows a $\sim$0.25 dex offset from the field (green solid star) in log([O III]/Hβ) and no log([N II]/Hα) offset. Binned and stacked AGNs are shown for reference (outlined black circle). Both proto-cluster samples are located in the same log([O III]/Hβ) range as the SDSS sample, and both field samples have values of log([O III]/Hβ) consistent with the Shapley et al. (2015) MOSDEF sample of $z \sim 2.3$ field galaxies (fuchsia dashed line).

4.2.3. Environment versus Mass

In order to disentangle the effects of environment and mass, we separate our proto-cluster and field sample by stellar mass in the bottom two panels of Figure 6. Our proto-cluster and field bins are binned into a low-mass (log($M_\star$) < 9.60, transparent small points) and high-mass (log($M_\star$) > 9.60, transparent large points) bin. The mass bins were chosen because it is the median mass of the stacked COSMOS sample.

We find no significant differences (within error) in the log ([O III]/Hβ) ratio within low-mass bins in both COSMOS and UDS. In UDS, this is a 0.24 dex offset, and in COSMOS 0.05 dex. In the COSMOS low-mass bin, there is a 0.18 dex offset in the log([N II]/Hα) ratio, at a 1σ significance.

In the high-mass bins, we find tentative offsets in the log ([O III]/Hβ) ratio at the level of 0.67 dex in UDS, and 0.15 dex in COSMOS. However, the significance of the difference is subject to small number statistics in the UDS field population, and the COSMOS cluster population. When the low- and high-mass bins are stacked using a different mass cutoff, the offsets change.

To analyze the effects of stellar mass binning, we compare these results with separating low- and high-mass galaxies at log($M_\star$) = 9.72, the median mass of the total UDS and COSMOS populations, and log($M_\star$) = 9.46, the median mass of the stacked COSMOS cluster galaxies. We find that at high-mass cuts, and a lower number of galaxies in the high-mass bins, the UDS low-mass field bin displays a 0.40 dex (2σ) log ([O III]/Hβ) ratio offset from the proto-cluster stack. As the mass cuts become lower, the [O III]/Hβ offset moves to within error (0.34 dex). In the high-mass bins we see the opposite effect, where at a smaller bin size and higher-mass cut, we see no significant offset (0.13 dex, within errors), and at a lower-mass cut we see a 2σ offset (0.68 dex).

Due to low numbers and high sky-noise levels in the Hβ emission line in the UDS field population, we consistently derive high errors for the high-mass field-stacked flux ratios. Therefore, the significance of any offset would be dependent on adding future data to the field bins. We still include these galaxies for a complete analysis.
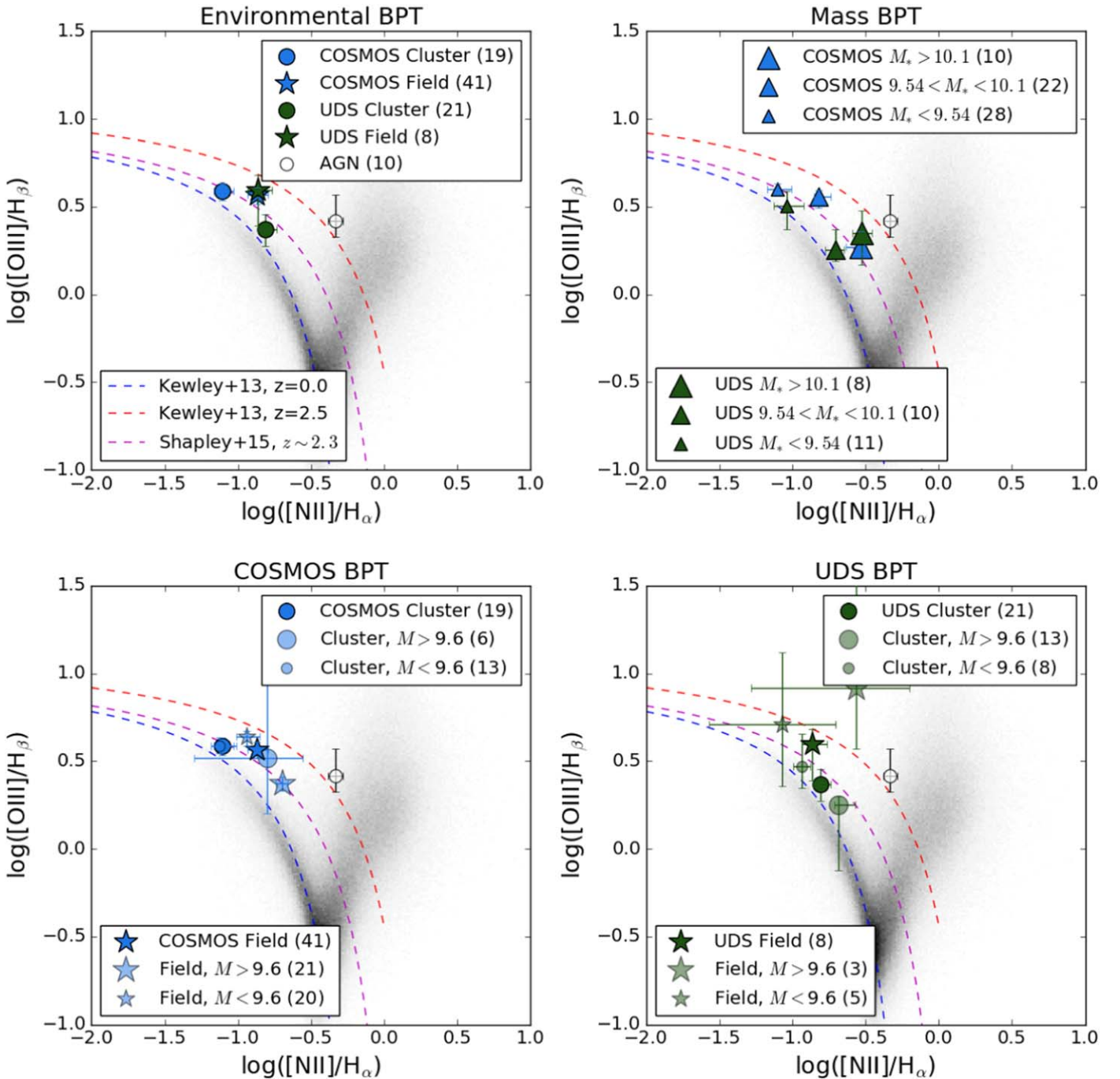
Figure 6. BPT diagram of galaxies within our two proto-clusters. We stack our galaxies according to their mass, environmental density, field (COSMOS or UDS), and inferred excitation mechanism (AGNs identified via radio, IR, UV, or BPT diagrams are separated from all stacks). Upper left panel: stacking according to field and environmental density, where we find an offset in the [N II]/Hα ratio in COSMOS, and the [O III]/Hβ ratio in UDS. Upper right panel: stacking according to FAST-inferred stellar mass. We find a stronger effect from stellar mass in both fields. Lower left panel: the COSMOS $z \sim 2$ sample, split into low- and high-mass bins in both proto-cluster and field. The low- and high-mass bins are split at $\log(M_\star) = 9.60$, which is the median of the COSMOS stacked sample. Lower right panel: the UDS sample similarly separated into high and low stellar-mass bins with respect to environment.

In the COSMOS data set, we find that at high-mass cuts, the low-mass COSMOS sample has no significant [O III]/Hβ off-sets (0.05 dex), but at lower-mass cuts, we see a 0.11 dex offset. The significance of this offset is questionable due to the high errors seen in the high-mass proto-cluster stack. The [N II]/Hα ratio displays the inverse correlation; at high-mass cuts, there is a 2σ offset (0.25 dex) and no offset at low-mass cuts. In the high-mass COSMOS stacks, we see large errors in the cluster bin due to low counts but a consistent offset in

[N II]/Hα ratio between cluster and field of around 3σ (0.22 dex).

We discuss the possible explanations for the [O III]/Hβ offset, if confirmed by larger data sets, in Section 5. However, we emphasize the speculative nature of the [O III]/Hβ ratio offset due to low bin counts and low number statistics. A larger sample of high-mass objects in both UDS and COSMOS would provide a more robust analysis of the log ([O III]/Hβ) offset.

5. Discussion

The ZFIRE survey was conducted to determine if and when a galaxy's environmental density at high redshift plays a role in the evolution of its observed properties (Tran et al. 2015; Alcorn et al. 2016). Multiple analyses focused on SFR (Koyama et al. 2013a, 2013b; Tran et al. 2015, 2017), metallicity (Kacprzak et al. 2015, 2016; Tran et al. 2015), ionized gas characteristics (Kewley et al. 2016), gas content (Koyama et al. 2017; Darvish et al. 2018), and kinematics (Alcorn et al. 2016, 2018) have shown that the proto-clusters observed at $z > 1.5$ have no significant environmental trends.

5.1. [O III]/Hβ Ratios and Environment

Despite previous non-detections of environmental effects on galaxy properties in the COSMOS proto-cluster at $z \sim 2.0.5$ (Kewley et al. 2016), we find a tentative environmental effect on galaxy [O III]/Hβ ratio when we stack high-mass galaxies (Section 3.2). However, depending on the mass cuts for the stacks, these offsets can disappear. The [O III]/Hβ ratio correlates with the ionization parameter, electron density, hardness of the ionizing field, and metallicity. If confirmed at a significance of 2σ with a larger data set, this offset would suggest that dense environment might have an effect on the ionized gas characteristics of a galaxy. However, these results are poorly constrained due to large errors and small number statistics, so further observations and longer exposures of these galaxies are necessary to confirm these results.

The [O III]/Hβ offset between cluster and field is seen in both the UDS and COSMOS populations at high mass (Section 4.2.1). However, we found that metallicity offsets were not correlated with environment, agreeing with prior studies (Section 4.1.2, Kacprzak et al. 2015; Tran et al. 2015). Taking these two results together suggests that field galaxies have a higher ionization parameter than proto-cluster galaxies in UDS, whereas proto-cluster galaxies in COSMOS have a higher ionization parameter than in the field (Kewley et al. 2015).

Additional metallicity diagnostics such as R_{23}, which utilizes [O III]4959,5007 Å and Hβ4861 Å fluxes, would be needed to confirm this result and rule out the choice of a strong-line metallicity indicator as the cause of null detection in metallicity. A change in the [O III]/Hβ ratio would not affect PP04 and D16 indicators, which only use Hα, [N II], and [S II] fluxes. In contrast, the R_{23} indicator would be affected by a change in the [O III]/Hβ ratio, as R_{23} is dependent on measurements of [O III] and the [O II] doublet fluxes. Our data set includes [O II]3727,29 Å fluxes for a limited number of objects, so R_{23} measurements are not performed but will be an important test of our results in the future.

6. Conclusions

We perform an analysis of the ionized gas and gas-phase metallicity of two over-dense regions: the UDS proto-cluster at $z = 1.62$ and COSMOS proto-cluster at $z = 2.095$. The rest-frame optical diagnostic lines Hβ, [O III], Hα, [N II], and [S II] are measured using the NIR spectrograph on Keck, MOSFIRE. Fluxes of these emission lines are extracted via a Gaussian fit to the 1D spectrum.

Absolute fluxes of Hα, [N II], and [S II] are used to calculate the gas-phase metallicity using the abundance indicator presented in Dopita et al. (2016) and to compare with the

metallicities derived using the method in Pettini & Pagel (2004). We find no gas-phase metallicity offsets between our two proto-clusters at differing redshifts or any metallicity enhancement relative to field galaxies at the redshifts of these galaxies. Our results are consistent with predictions from IllustrisTNG (Gupta et al. 2018; Torrey et al. 2018). We compare the utility of the PP04 and D16 indicators and find that low [S II] fluxes and high sky interference limit the use of the D16 indicator for our $z = 1.6$ and $z = 2.1$ samples due to high scatter ($\sim$0.5 dex).

For the subset of galaxies where all four diagnostic lines are measured, we analyze the nebular gas properties using the BPT diagram. We find an offset in the [O III]/Hβ ratio, or the ionization parameter in each population from the local SDSS sample. The offset is consistent with photoionization models at high redshift, due to increasingly extreme ISM conditions (e.g., higher ionization parameter, higher electron density, harder ionizing field; Kewley et al. 2013, 2015). When objects are stacked, we find a tentative 1–2σ log([O III]/Hβ) enhancement in high-mass ($>\log(M_\star) = 9.60$) field galaxies in the UDS stacks compared to high-mass proto-cluster galaxies.

Further observations of over-dense regions of galaxies at $z \sim 2$ are needed to determine the significance of our results. In particular, larger sample sizes are needed in low-sky emission redshift windows or with longer integration times so that [S II] emission-line fluxes are better constrained. Additionally, more measurements of clusters and proto-clusters at $z \sim 1.0$–1.5 are needed, where IllustrisTNG predicts a metallicity enhancement relative to the field. Likewise, cosmological simulations need to predict how ionization parameters and nebular gas properties change with environment.

ORCID iDs

Leo Y. Alcorn ⓘ https://orcid.org/0000-0002-2250-8687
Anshu Gupta ⓘ https://orcid.org/0000-0002-8984-3666
Kim-Vy Tran ⓘ https://orcid.org/0000-0001-9208-2143
Glenn G. Kacprzak ⓘ https://orcid.org/0000-0003-1362-9302
Tiantian Yuan ⓘ https://orcid.org/0000-0002-9211-3277
Jonathan Cohn ⓘ https://orcid.org/0000-0003-1420-6037
Ben Forrest ⓘ https://orcid.org/0000-0001-6003-0541

Karl Glazebrook ⬤ https://orcid.org/0000-0002-3254-9044
Lisa J. Kewley ⬤ https://orcid.org/0000-0001-8152-3943
Ivo Labbé ⬤ https://orcid.org/0000-0002-2057-5376
Themiya Nanayakkara ⬤ https://orcid.org/0000-0003-2804-0648
Casey Papovich ⬤ https://orcid.org/0000-0001-7503-8482
Lee R. Spitler ⬤ https://orcid.org/0000-0001-5185-9876
Caroline M. S. Straatman ⬤ https://orcid.org/0000-0001-5937-4590

References

Alcorn, L. Y., Tran, K.-V., Glazebrook, K., et al. 2018, ApJ, 858, 47
Alcorn, L. Y., Tran, K.-V. H., Kacprzak, G. G., et al. 2016, ApJL, 825, L2
Allen, R. J., Kacprzak, G. G., Spitler, L. R., et al. 2015, ApJ, 806, 3
Baldwin, J. A., Phillips, M. M., & Terlevich, R. 1981, PASP, 93, 5
Bassett, R., Papovich, C., Lotz, J. M., et al. 2013, ApJ, 770, 58
Blanton, M. R., Eisenstein, D., Hogg, D. W., Schlegel, D. J., & Brinkmann, J. 2005, ApJ, 629, 143
Brinchmann, J., Pettini, M., & Charlot, S. 2008, MNRAS, 385, 769
Bruzual, G., & Charlot, S. 2003, MNRAS, 344, 1000
Calzetti, D., Armus, L., Bohlin, R. C., et al. 2000, ApJ, 533, 682
Cappellari, M., Emsellem, E., Krajnović, D., et al. 2011, MNRAS, 416, 1680
Chabrier, G. 2003, PASP, 115, 763
Cooper, M. C., Newman, J. A., Croton, D. J., et al. 2006, MNRAS, 370, 198
Cooper, M. C., Tremonti, C. A., Newman, J. A., & Zabludoff, A. I. 2008, MNRAS, 390, 245
Cowley, M. J., Spitler, L. R., Tran, K.-V. H., et al. 2016, MNRAS, 457, 629
Darvish, B., Scoville, N. Z., Martin, C., et al. 2018, ApJ, 860, 111
Davé, R., Finlator, K., & Oppenheimer, B. D. 2011, MNRAS, 416, 1354
Dopita, M. A., Kewley, L. J., Sutherland, R. S., & Nicholls, D. C. 2016, APSS, 361, 61
Ellison, S. L., Simard, L., Cowan, N. B., et al. 2009, MNRAS, 396, 1257
Gobat, R., Daddi, E., Onodera, M., et al. 2011, A&A, 526, A133
Grootes, M. W., Tuffs, R. J., Popescu, C. C., et al. 2017, AJ, 153, 111
Gupta, A., Yuan, T., Torrey, P., et al. 2018, MNRAS, 477, L35
Hatch, N. A., Kurk, J. D., Pentericci, L., et al. 2011, MNRAS, 415, 2993
Hopkins, A. M., & Beacom, J. F. 2006, ApJ, 651, 142
Houghton, R. C. W. 2015, MNRAS, 451, 3427
Ito, K., Kashikawa, N., Toshikawa, J., et al. 2019, ApJ, 878, 68
Jarrett, T. H., Cluver, M. E., Magoulas, C., et al. 2017, ApJ, 836, 182
Kaasinen, M., Kewley, L., Bian, F., et al. 2018, MNRAS, 477, 5568
Kacprzak, G. G., van de Voort, F., Glazebrook, K., et al. 2016, ApJL, 826, L11
Kacprzak, G. G., Yuan, T., Nanayakkara, T., et al. 2015, ApJL, 802, L26
Kawinwanichakij, L., Papovich, C., Quadri, R. F., et al. 2017, ApJ, 847, 134
Kewley, L. J., Dopita, M. A., Leitherer, C., et al. 2013, ApJ, 774, 100
Kewley, L. J., & Ellison, S. L. 2008, ApJ, 681, 1183
Kewley, L. J., Yuan, T., Nanayakkara, T., et al. 2016, ApJ, 819, 100
Kewley, L. J., Zahid, H. J., Geller, M. J., et al. 2015, ApJL, 812, L20
Kobayashi, C., Springel, V., & White, S. D. M. 2007, MNRAS, 376, 1465
Koyama, S., Koyama, Y., Yamashita, T., et al. 2017, ApJ, 847, 137
Koyama, Y., Kodama, T., Tadaki, K.-i., et al. 2013a, MNRAS, 428, 1551
Koyama, Y., Smail, I., Kurk, J., et al. 2013b, MNRAS, 434, 423
Kriek, M., van Dokkum, P. G., Labbé, I., et al. 2009, ApJ, 700, 221
Kulas, K. R., McLean, I. S., Shapley, A. E., et al. 2013, ApJ, 774, 130
Lawrence, A., Warren, S. J., Almaini, O., et al. 2007, MNRAS, 379, 1599
Lee, S.-K., Im, M., Kim, J.-W., et al. 2015, ApJ, 810, 90
Lehnert, M. D., Nesvadba, N. P. H., Le Tiran, L., et al. 2009, ApJ, 699, 1660
Lewis, I., Balogh, M., De Propris, R., et al. 2002, MNRAS, 334, 673
Liu, X., Shapley, A. E., Coil, A. L., Brinchmann, J., & Ma, C.-P. 2008, ApJ, 678, 758
Lotz, J. M., Papovich, C., Faber, S. M., et al. 2013, ApJ, 773, 154
Madau, P., & Dickinson, M. 2014, ARA&A, 52, 415
Magrini, L., Sommariva, V., Cresci, G., et al. 2012, MNRAS, 426, 1195
Maiolino, R., & Mannucci, F. 2019, A&ARv, 27, 3
Nanayakkara, T., Glazebrook, K., Kacprzak, G. G., et al. 2016, ApJ, 828, 21
Nantais, J. B., Rettura, A., Lidman, C., et al. 2013, A&A, 556, A112
Newman, S. F., Buschkamp, P., Genzel, R., et al. 2014, ApJ, 781, 21
Newman, S. F., Shapiro Griffin, K., Genzel, R., et al. 2012, ApJ, 752, 111
Paalvast, M., Verhamme, A., Straka, L. A., et al. 2018, A&A, 618, A40
Papovich, C., Bassett, R., Lotz, J. M., et al. 2012, ApJ, 750, 93
Papovich, C., Momcheva, I., Willmer, C. N. A., et al. 2010, ApJ, 716, 1503
Pettini, M., & Pagel, B. E. J. 2004, MNRAS, 348, L59
Pilyugin, L. S., & Mattsson, L. 2011, MNRAS, 412, 1145
Pilyugin, L. S., & Thuan, T. X. 2005, ApJ, 631, 231
Pintos-Castro, I., Yee, H. K. C., Muzzin, A., Old, L., & Wilson, G. 2019, ApJ, 876, 40
Rettura, A., Rosati, P., Nonino, M., et al. 2010, ApJ, 709, 512
Sanders, R. L., Shapley, A. E., Kriek, M., et al. 2015, ApJ, 799, 138
Sanders, R. L., Shapley, A. E., Kriek, M., et al. 2018, ApJ, 858, 99
Shapley, A. E., Reddy, N. A., Kriek, M., et al. 2015, ApJ, 801, 88
Shimakawa, R., Kodama, T., Hayashi, M., et al. 2018, MNRAS, 473, 1977
Shimakawa, R., Kodama, T., Tadaki, K., et al. 2015, MNRAS, 448, 666
Shirazi, M., Brinchmann, J., & Rahmati, A. 2014, ApJ, 787, 120
Spitler, L. R., Labbé, I., Glazebrook, K., et al. 2012, ApJL, 748, L21
Steidel, C. C., Rudie, G. C., Strom, A. L., et al. 2014, ApJ, 795, 165
Steidel, C. C., Strom, A. L., Pettini, M., et al. 2016, ApJ, 826, 159
Straatman, C. M. S., Spitler, L. R., Quadri, R. F., et al. 2016, ApJ, 830, 51
Strazzullo, V., Daddi, E., Gobat, R., et al. 2016, ApJL, 833, L20
Suzuki, T. L., Minowa, Y., Koyama, Y., et al. 2019, PASJ, 71, 69
Tacconi, L. J., Neri, R., Genzel, R., et al. 2013, ApJ, 768, 74
Tanaka, M., Finoguenov, A., & Ueda, Y. 2010, ApJL, 716, L152
Telford, O. G., Dalcanton, J. J., Skillman, E. D., & Conroy, C. 2016, ApJ, 827, 35
Torrey, P., Vogelsberger, M., Hernquist, L., et al. 2018, MNRAS, 477, L16
Tran, K.-V. H., Alcorn, L. Y., Kacprzak, G. G., et al. 2017, ApJ, 834, 101
Tran, K.-V. H., Nanayakkara, T., Yuan, T., et al. 2015, ApJ, 811, 28
Tran, K.-V. H., Papovich, C., Saintonge, A., et al. 2010, ApJL, 719, L126
Valentino, F., Daddi, E., Strazzullo, V., et al. 2015, ApJ, 801, 132
Watson, C., Tran, K.-V., Tomczak, A., et al. 2019, ApJ, 874, 63
Williams, R. J., Quadri, R. F., Franx, M., van Dokkum, P., & Labbé, I. 2009, ApJ, 691, 1879
Wuyts, E., Kurk, J., Förster Schreiber, N. M., et al. 2014, ApJL, 789, L40
Yuan, T., Nanayakkara, T., Kacprzak, G. G., et al. 2014, ApJL, 795, L20
Zahid, H. J., Kashino, D., Silverman, J. D., et al. 2014, ApJ, 792, 75